



1 **Unveiling the multiphase fate of 2,4-dinitrophenol on**  
2 **aerosols: Interfacial hydration governs competing oxi-**  
3 **dation pathways and unexpected toxicity amplification**

4

5

6 Chenlei Wang<sup>1</sup>, Ran Li<sup>1</sup>, Jiaying Sun<sup>2</sup>, Zihan Zhang<sup>1</sup>, Nan Zhao<sup>1</sup>, Leilei Liu<sup>\*1</sup>, Zuju

7

Ma<sup>1</sup>, Maoxia He<sup>3</sup>, Jianfei Sun<sup>\*1</sup>

8

<sup>1</sup>School of Environmental and Material Engineering, Yantai University,

9

Yantai 264005, P. R. China

10

<sup>2</sup>Shandong Pengbo Safety & Environmental Services Limited, Yantai 265600, P. R.

11

China

12

<sup>3</sup>Environment Research Institute, Shandong University,

13

Qingdao 266237, P. R. China

14

15

16

17 **Keywords:** Phenols; Multi-oxidant; Solvation effect; Density functional theory; Bio-

18 **toxicity**

19

20 *\*Corresponding author.* E-mail: Jianfei Sun: jianfeisun@ytu.edu.cn

21

Leilei Liu: liuleileimail@163.com



22 **Abstract**

23 This study elucidates the atmospheric transformation mechanisms of 2,4-dinitro-  
24 phenol (2,4-DNP) using an integrated computational framework. Initial oxidation by  
25 hydroxyl radicals ( $\bullet\text{OH}$ ) and ozone ( $\text{O}_3$ ) was identified as the dominant pathway,  
26 whereas the direct reaction with nitrogen dioxide radical ( $\bullet\text{NO}_2$ ) is kinetically hindered.  
27 A key mechanistic insight is that these primary reactions are inhibited by solvation ef-  
28 fects, while nitro substituents further suppress the reaction rates, establishing a quanti-  
29 tative link between electronic structure and degradation kinetics. The subsequent at-  
30 mospheric fate of the radical intermediate is governed by hydrogen atom abstraction  
31 (HAA) reactions with ambient oxygen ( $\text{O}_2$ ) and  $\bullet\text{NO}_2$ . Molecular dynamics (MD) sim-  
32 ulations demonstrate that the adsorption of 2,4-DNP onto aerosol surrogates is non-  
33 monotonically modulated by interfacial hydration. Crucially, computational toxicology  
34 predicts that the ozonolysis process amplifies, rather than mitigates, environmental risk  
35 by generating secondary products with significantly enhanced mutagenicity and devel-  
36 opmental toxicity. These findings provide mechanistic insights into the environmental  
37 risk amplification associated with nitroaromatic compounds and highlight the necessity  
38 of evaluating toxic transformation products for accurate environmental risk assessment.



## 39 **1 Introduction**

40 Atmospheric aerosols, as pivotal regulators of the Earth's climate system and en-  
41 vironmental quality, have long placed the complex study of their physicochemical pro-  
42 cesses at the forefront of scientific inquiry (Perumpully and Gautam, 2025; McNeill,  
43 2017). Among them, secondary organic aerosols (SOAs) exert substantial influences  
44 on the global radiation balance and public health (Li et al., 2022a; Kroll and Seinfeld,  
45 2008). Their formation originates from the oxidation, nitration, and subsequent reac-  
46 tions of volatile organic compounds (VOCs), which generate semi-volatile and low-  
47 volatility products (Fan et al., 2022; Li et al., 2021; Mahilang et al., 2021). Within the  
48 diverse range of precursors, nitrophenolic compounds (NPs) have attracted considera-  
49 ble attention because of their strong light-absorbing properties, inherent biological tox-  
50 icity, and potential role as important SOA precursors (Li et al., 2022b; Li et al., 2020;  
51 Salvador et al., 2021). As a representative nitrated aromatic compound, 2,4-dinitrophe-  
52 nol (2,4-DNP) is widely present in industrial emissions and can also be formed through  
53 atmospheric secondary reactions, posing considerable environmental risks (Shukla et al.,  
54 2009; Yan et al., 2021).

55 However, accurately assessing the environmental risks of nitrophenolic pollutants  
56 and predicting their fate requires more than identifying their large-scale sources and  
57 impacts. The key lies in elucidating their specific chemical transformation mechanisms  
58 in the atmosphere. Current understanding of the degradation mechanisms of organic  
59 compounds mainly focuses on homogeneous reactions, particularly daytime photo-  
60 chemical oxidation pathways dominated by  $\bullet\text{OH}$  (Schaefer and Herrmann, 2018; Hu et



61 al., 2021; Liu et al., 2023). In reality, a significant fraction of atmospheric reactions  
62 occurs at the heterogeneous interfaces of aerosols or droplets, a process that is espe-  
63 cially crucial at night and under highly polluted conditions(Xing et al., 2019). At these  
64 interfaces, the molecular orientation of pollutants, the local solvation environment, par-  
65 ticularly the structure of water molecules and interactions with particle surfaces collec-  
66 tively reshape their reactivity and pathways, potentially even dictating their ultimate  
67 environmental fate(Ohto et al., 2019; Mao et al., 2024; Lee et al., 2014). Consequently,  
68 selecting a model system that can effectively represent the surface characteristics of  
69 real atmospheric carbonaceous particles is of great importance. Fullerene (C<sub>60</sub>), owing  
70 to its well-defined, stable carbon cage structure and abundant  $\pi$ -electron cloud, provides  
71 an ideal model for studying non-covalent interactions at organic compound-particle in-  
72 terfaces(Athar and Patnaik, 2022; Liu and Lu, 2024). This offers a clear platform for  
73 probing the molecular-level regulatory role of interfacial hydration.

74 In the complex and dynamic real atmosphere, interfacial chemical transformations  
75 constitute a competitive and evolving process. A comprehensive understanding of the  
76 atmospheric behavior of nitroaromatic compounds requires moving beyond the tradi-  
77 tional isolated study of single static oxidation pathways. Instead, it requires a perspec-  
78 tive that considers their fate within a dynamic network driven by multiple reactive spe-  
79 cies(Thangamani et al., 2016). The key drivers of this network are three core atmos-  
80 pheric oxidants whose relative importance varies with environmental conditions(Sun et  
81 al., 2021). These include the primary daytime oxidant  $\bullet$ OH, O<sub>3</sub> with its high background  
82 concentration and strong oxidizing capacity, and  $\bullet$ NO<sub>2</sub>, which can accumulate at night



83 in polluted regions and initiate non-photochemical nitration pathways(Delaria and Co-  
84 hen, 2023; Pillar et al., 2014; Yang et al., 2023b). Differences in the concentrations,  
85 reactivities, and reaction mechanisms of these species collectively shape the diverse  
86 transformation pathways of nitroaromatics across diurnal cycles and under varying pol-  
87 lution regimes.

88 Notably, such multi-pathway transformation processes generate a series of inter-  
89 mediates and final products with diverse chemical properties, which can fundamentally  
90 alter the ecological risk profile of nitroaromatic pollutants(Tiwari et al., 2019; Tam et  
91 al., 2021). Taking 2,4-DNP as an example, it exhibits not only acute toxicity but also  
92 potential for bioaccumulation and genotoxicity, thereby posing a long-term ecological  
93 threat through food-chain amplification(Ahmaruzzaman et al., 2024; Mangotra and  
94 Singh, 2024; Grundlingh et al., 2011). However, traditional experimental approaches  
95 often struggle to comprehensively identify all reactive intermediates and transformation  
96 products, and are frequently inadequate for efficiently evaluating their toxicological  
97 effects(Tam et al., 2021; Vom Eyser et al., 2013).

98 To address these gaps, this study employs an integrated multiscale theoretical  
99 framework combining density functional theory (DFT), molecular dynamics (MD) sim-  
100 ulations, and computational toxicology to investigate the competing oxidation and ni-  
101 tration pathways of 2,4-DNP in gas and aqueous phases, its interfacial adsorption be-  
102 havior on carbonaceous aerosol surrogates under different hydration, and the toxicity  
103 evolution of its transformation products. The results provide mechanistic insights into



104 the multiphase fate of nitrated aromatics and highlight the importance of evaluating  
105 toxic intermediates in atmospheric risk assessment.

## 106 **2 Computational methods**

### 107 **2.1 Density functional theory**

108 All density functional theory calculations in this study were performed using the  
109 Gaussian 16 software package(Frisch et al., 2016). Geometry optimization, frequency  
110 analysis, and single-point energy calculations were conducted for all structures along  
111 the reaction pathway, including reactants (Rs), transition states (TSs), intermediates  
112 (IMs), and products (Ps), employing the M06-2X functional(Zhao and Truhlar, 2008).  
113 To validate the reliability of the chosen basis set, the representative reaction 2,4-DNP  
114 + •OH → IM3 was selected, and reaction energies using multiple basis sets were sys-  
115 tematically compared, as summarized in Table S1 of the Supplement. The results indi-  
116 cated that the exothermicity computed with different basis sets are in excellent agree-  
117 ment. Among the tested combinations, M06-2X/6-311++G(3df,2p) level yields reac-  
118 tion energies closest to the high-accuracy CCSD(T) benchmark(Spiegel et al., 2024;  
119 Nagy, 2024). Considering both computational accuracy and efficiency, the composite  
120 method M06-2X/6-31+G(d,p)//6-311++G(3df,2p) was consistently applied in all sub-  
121 sequent calculations. Transition states were located using the TS optimization algo-  
122 rithm and further validated through vibrational frequency analysis and intrinsic reaction  
123 coordinate (IRC) calculations(Maeda et al., 2015). Frequency analysis confirmed that  
124 all stable structures exhibit no imaginary frequencies, while each transition state pos-  
125 sesses exactly one imaginary frequency, consistent with the characteristics of a first-



126 order saddle point, thereby validating the reaction pathway. The IRC trajectories for  
127 key transition states are shown in Figure S1. In addition, the solvation model based on  
128 density (SMD)(Kromann et al., 2018) was employed to analyze the electronic structures,  
129 reactive sites, and free energy changes of key molecules in solvated states.

130 To gain deeper insights into the ground-state electronic structure and the delocal-  
131 ization characteristics of potential reactive sites, orbital-weighted dual descriptor  
132 (OWDD)(Pino-Rios et al., 2019) analysis was conducted using the Multiwfn pro-  
133 gram(Lu and Chen, 2012). Furthermore, the independent gradient model (IGM) ap-  
134 proach was employed to systematically examine both chemical bonding and noncova-  
135 lent weak interactions within the system(Lefebvre et al., 2017; Lu and Chen, 2022).

## 136 **2.2 Molecular dynamics simulations**

137 All MD simulations were performed using the GROMACS 2018.8 software pack-  
138 age(Van Der Spoel et al., 2005). The simulation system was constructed within a peri-  
139 odic boundary box measuring  $30 \text{ \AA} \times 30 \text{ \AA} \times 60 \text{ \AA}$ . Each system contained 6 C60 mol-  
140 ecules and 15 2,4-DNP molecules, solvated with varying numbers of water molecules  
141 (100, 200, 300, and 400), using the explicit SPC/E water model. To mimic a realistic  
142 aerosol multiphase interface, a  $20 \text{ \AA}$  vacuum layer was introduced along the z-axis to  
143 create an explicit air-water interface.

144 The AMBER99SB-ILDN force field was employed for C60 and water molecules,  
145 whereas the generalized AMBER force field (GAFF) was used to parameterize 2,4-  
146 DNP(Shirts et al., 2003). All topology files were generated with the interactive sobtop



147 program(Lu, 2026). Prior to production runs, each system underwent energy minimi-  
148 zation to eliminate unfavorable atomic overlaps. The systems were subsequently equil-  
149 ibrated for 500 ps in the NVT ensemble at 298.15 K with a 2 fs integration time step,  
150 followed by production MD simulations of 1 ns for data collection and analysis. All  
151 molecular visualizations and trajectory analyses were performed using the VMD soft-  
152 ware(Humphrey et al., 1996).

### 153 **2.3 Kinetic calculations**

154 The rate constants for the primary reactions were calculated using the thermody-  
155 namic formulation of the conventional transition state theory (TST)(Tuñón and Wil-  
156 liams, 2019) with support from the KIShelp tool(Canneaux et al., 2014) and TST cal-  
157 culator(Lu, 2025), as represented by the following equation:

$$158 \quad k^{\text{TST}} = \sigma^* k_B T / h^* e^{-\Delta G^\ddagger / (k_B T)} \quad (1)$$

159 where  $\sigma$  is the reaction path degeneracy,  $k_B$  is the Boltzmann constant,  $T$  is the temper-  
160 ature, and  $h$  is Planck's constant.  $\Delta G^\ddagger$  represents the standard Gibbs free energy of  
161 activation for the considered reaction. For reaction path simplicity, the following equa-  
162 tion is followed:

$$163 \quad \sigma = \sigma_{rot, R} / \sigma_{rot, TS} \quad (2)$$

164 where  $\sigma_{rot, R}$  and  $\sigma_{rot, TS}$  are rotational symmetry numbers of reactants and transition  
165 states (for N molecule reactions,  $\sigma_{rot, R}$  is the product of the rotational symmetry num-  
166 bers of all the reactants);  $\sigma$  is generally 1 for reactions of macromolecular systems.

### 167 **2.4 Computational toxicology**



168 The toxicological profiles of 2,4-DNP and its atmospheric transformation products  
169 were characterized through a hierarchical quantitative structure activity relationship  
170 (QSAR) strategy(Young et al., 2008). Key toxicity endpoints, including Ames muta-  
171 genicity(Sushko et al., 2010) and developmental toxicity(Cassano et al., 2010), were  
172 predicted using the Toxicity Estimation Software Tool (T.E.S.T.) version 5.1.2 devel-  
173 oped by the U.S. Environmental Protection Agency(Epa, 2020). All predictions were  
174 subjected to applicability domain verification based on descriptor leverage analysis,  
175 and only data for compounds falling within the chemical space defined by the training  
176 set were retained to ensure the statistical validity and reliability of subsequent compar-  
177 ative toxicological analyses(Benfenati et al., 2009).

### 178 **3 Results and discussion**

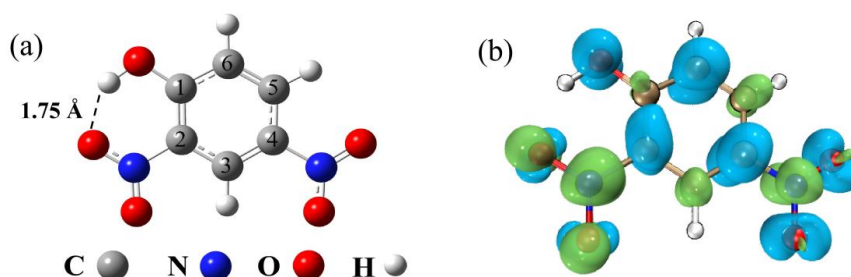
#### 179 **3.1 Reaction mechanisms of 2,4-DNP with O<sub>3</sub>, •OH, and •NO<sub>2</sub> in the gas and aque-** 180 **ous phases**

181 Establishing the stable molecular configuration and regional reactivity of 2,4-DNP  
182 is essential for understanding the initial reaction mechanisms with O<sub>3</sub> (an electrophile),  
183 •OH (a radical), and •NO<sub>2</sub> (which exhibits both electrophilic and radical characteristics).  
184 Such characterization provides critical theoretical insights into the distinct mechanistic  
185 origins of these reaction processes. To elucidate the fundamental reaction pathways and  
186 selectivity differences of 2,4-DNP with various reactants in multiphase environments,  
187 this study initiates a theoretical characterization of its ground state, including its elec-  
188 tronic structure and reactive sites.

##### 189 **3.1.1 Characterization of the electronic structure of 2,4-DNP**



190 Based on geometric optimization and electronic structure calculations, the stable  
191 conformation of 2,4-DNP and its reactive sites analysis are shown in Figure 1. The  
192 global minimum energy conformation stabilized by intramolecular hydrogen bonding  
193 is presented in Figure 1a, while the OWDD isosurface in Figure 1b clearly delineates  
194 the nucleophilic and electrophilic reaction regions of the molecule, thus providing a  
195 robust theoretical foundation for elucidating the subsequent reaction mechanisms.



196

197 **Figure 1** (a) The most stable configuration of 2,4-DNP, stabilized by intramolecular  
198 hydrogen bonding. (b) Isosurface of the OWDD for 2,4-DNP, where blue and red re-  
199 gions denote nucleophilic and electrophilic sites, respectively.

200 The global minimum energy conformation of 2,4-DNP is depicted in Figure 1a,  
201 with an electronic energy of  $-449508.49 \text{ kcal mol}^{-1}$ . The exceptional stability of this  
202 structure arises primarily from the synergistic effects of intramolecular hydrogen bond-  
203 ing and  $\pi$ -electron delocalization. Structural analysis indicates that a strong intramolec-  
204 ular hydrogen bond ( $\text{O}-\text{H}\cdots\text{O}-\text{N}$ ) between the hydroxyl group and the ortho-positioned  
205 nitro group (position 2), with a bond length of  $1.75 \text{ \AA}$ —a value characteristic of strong  
206 intramolecular hydrogen bonds ( $1.6\text{--}1.9 \text{ \AA}$ )(Steiner, 2002). This interaction forms a  
207 stable six-membered ring motif, which closely resembles the strain-free chair confor-  
208 mation of cyclohexane and thus provides optimal stabilization(Barton and Cookson,



1956). This hydrogen bond contributes substantial stabilization energy and constitutes  
the principal factor governing conformational preference. Additionally, both the ortho-  
and para-nitro groups (at positions 2 and 4, respectively) adopt nearly coplanar orientations relative to the benzene ring, with dihedral angles of  $178.30^\circ$  and  $179.67^\circ$ , approaching the ideal  $180^\circ$  for maximum orbital overlap. Importantly, thereby enabling effective p- $\pi$  conjugation with the aromatic  $\pi$  system and further enhancing the overall molecular stability (Szatylowicz et al., 2017). Importantly, these two stabilizing factors are mutually reinforcing: the hydrogen bond locks the ortho-nitro group into the plane, facilitating conjugation, while the enhanced conjugation further polarizes the nitro group, strengthening the hydrogen bond.

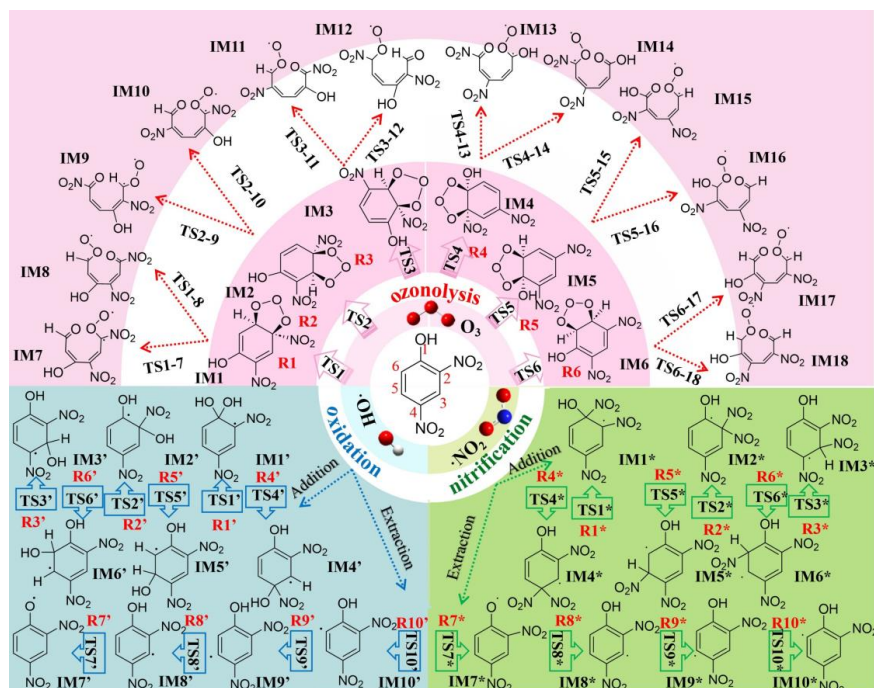
As shown in Figure 1b, the OWDD isosurface analysis ( $\Delta f\omega$ ) reveals well-defined regional chemical features of the 2,4-DNP. Blue regions ( $\Delta f\omega < 0$ ) are localized around specific carbon atoms on the benzene ring and the hydroxyl oxygen atom, indicating sites rich in lone electron pairs and thus prone to nucleophilic attack. These nucleophilic sites arise from the electron-donating effect of the hydroxyl group, which concentrates electron density at the ortho and para positions relative to the nitro groups. In contrast, green regions ( $\Delta f\omega > 0$ ) are mainly located at the outer ends of the oxygen and nitrogen atoms in the nitro and hydroxyl groups, showing electrophilic features associated with  $\sigma$ -hole interactions caused by the polarization of N-O and O-H bonds. This electronic structure feature provides a reliable prediction for predicting its reactivity toward various atmospheric oxidants. As a strong electrophile,  $O_3$  preferentially targets the electron-rich carbon atoms (blue regions), initiating electrophilic addition at the sites



231 with the highest nucleophilic character. Meanwhile,  $\bullet\text{OH}$  displays dual reactivity: it  
232 adds to nucleophilic blue regions on the benzene ring, while also abstracting hydrogen  
233 atoms from weakly electrophilic sites such as the C–H bonds (adjacent to nitro groups)  
234 or the hydroxyl hydrogen, which correspond to regions of weaker  $\Delta f\omega$  positive values.  
235 Similarly,  $\bullet\text{NO}_2$ , possessing both radical and electrophilic characteristics, displays dual  
236 reactivity, participating either in radical addition to nucleophilic carbons or in hydrogen  
237 abstraction reactions, with its preference modulated by the local  $\Delta f\omega$  distribution.

### 238 **3.1.2 Primary reactions of 2,4-DNP with $\text{O}_3$ , $\bullet\text{OH}$ , and $\bullet\text{NO}_2$**

239 Based on the analysis of nucleophilic and electrophilic sites in the electronic struc-  
240 ture of 2,4-DNP, this section systematically elaborates the primary reaction pathways  
241 of 2,4-DNP with  $\text{O}_3$ ,  $\bullet\text{OH}$ , and  $\bullet\text{NO}_2$ . The competition among different channels is elu-  
242 cidated through thermodynamic and kinetic calculations, thereby revealing transfor-  
243 mation mechanisms of 2,4-DNP in the atmosphere.



244

245 **Figure 2** Proposed initial reaction mechanisms of 2,4-DNP with  $O_3$ ,  $\bullet OH$ , and  $\bullet NO_2$ .

246 The coexistence of an electron-donating hydroxyl group and strong electron-with-  
 247 drawing nitro groups in the 2,4-DNP induces a highly polarized and asymmetric distri-  
 248 bution of  $\pi$ -electron density in the benzene ring (Li et al., 2023). This distinct electronic  
 249 structure directly governs the pronounced regioselectivity of its reactions with  $O_3$ ,  $\bullet OH$ ,  
 250 and  $\bullet NO_2$ .

251 As a typical 1,3-dipole, ozone can attack the electron-rich aromatic  $\pi$ -system via  
 252 cycloaddition. Calculations indicate that among the six possible 1,3-dipolar cycloaddi-  
 253 tion pathways, the reaction preferentially occurs at the C5–C6 bond located between  
 254 the hydroxyl and nitro groups, as indicated by the red region in Figure 2. The reaction  
 255 proceeds via transition state TS6, in which the terminal oxygen atoms of  $O_3$  (O1 and  
 256 O3) simultaneously approach the C5 and C6 atoms. The forming C5–O1 and C6–O3



257 bonds reach lengths of 1.43 Å and 1.42 Å, respectively, while the original C5–C6 dou-  
258 ble bond is significantly elongated from 1.38 Å to 1.56 Å, indicating irreversible dis-  
259 ruption of aromatic stabilization. This step represents the most favorable reaction path-  
260 way. Subsequently, the resulting unstable primary ozonide (POZ) intermediate IM6 un-  
261 dergoes concerted dissociation via transition state TS6-17. During this process, the O2–  
262 O3 bond elongates to 2.02 Å, and the C5–C6 bond extends to 1.96 Å, while new C5–  
263 O1 and C6–O3 bonds begin to form with lengths of approximately 1.32 Å and 1.26 Å,  
264 respectively. This leads to the formation of the vibrationally excited Criegee interme-  
265 diate (CI) IM17, which is energetically the most favorable product.

266 The reaction of 2,4-DNP with •OH mainly proceeds through two competing mech-  
267 anisms, namely ring addition and HAA, as shown in the blue region of Figure 2. In the  
268 electrophilic addition pathway, •OH preferentially attacks the C3 site, which is located  
269 between the two nitro groups and is meta to the hydroxyl substituent. This process pro-  
270 ceeds through transition state TS3', where the distance between the oxygen atom of  
271 •OH and C3 decreases to 1.42 Å (from an initial separation of 1.99 Å). Concurrently,  
272 the C2–C3 and C3–C4 bond lengths increase from 1.40 Å to 1.50 Å, indicating signif-  
273 icant disruption of the local aromatic structure and a redistribution of  $\pi$ -bonding within  
274 the ring. The O–H bond of •OH forms an angle of approximately 110° with the plane  
275 of the aromatic ring, a geometry that facilitates effective overlap between the p-orbital  
276 of •OH and the  $\pi$ -system of the benzene ring, thereby promoting  $\sigma$ -bond formation and  
277 ultimately yielding the hydroxycyclohexadienyl radical intermediate IM3'. In the HAA



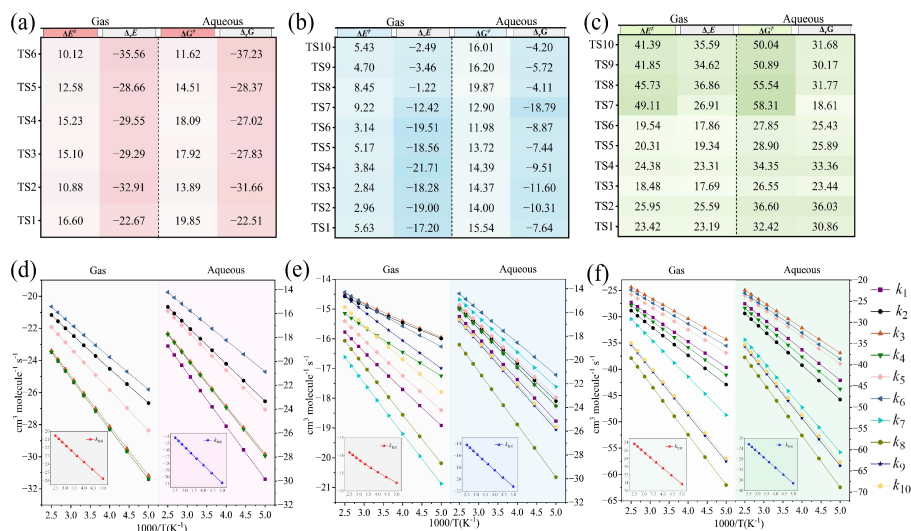
278 pathway,  $\bullet\text{OH}$  primarily captures the H atom directly bonded to the C5 site. This reac-  
279 tion proceeds through transition state TS9', in which the distance between the oxygen  
280 atom of  $\bullet\text{OH}$  and the hydrogen on C5 shortens to 1.19 Å, the breaking C5–H bond  
281 elongates from 1.08 Å to 1.26 Å, and the O–H–C5 angle approaches 179°, which is  
282 characteristic of a hydrogen-abstraction transition state. This step produces the phenoxy  
283 radical intermediate IM9' and one molecule of H<sub>2</sub>O. Notably, the OWDD analysis in-  
284 dicates that the carbon at C5 exhibits electrophilic character (low electron density). This  
285 is contrary to the conventional expectation for hydrogen abstraction by an electrophilic  
286 radical such as  $\bullet\text{OH}$ . Nevertheless, the calculations show that this site remains the dom-  
287 inant abstraction site in the HAA pathway. This selectivity shift suggests that the HAA  
288 reaction of  $\bullet\text{OH}$  may be governed by bond-strength control and transition-state electro-  
289 static complementarity, rather than being determined solely by ground-state electro-  
290 phile–nucleophile interactions. Indeed, the C–H bond dissociation energy has been es-  
291 tablished as a key factor controlling the site-selectivity of HAA by  $\bullet\text{OH}$ , with weaker  
292 bonds being preferentially abstracted.

293 The green region in Figure 2 illustrates the reaction mechanism of  $\bullet\text{NO}_2$  with 2,4-  
294 DNP. Although the reaction pathways of 2,4-DNP with  $\bullet\text{NO}_2$  and  $\bullet\text{OH}$  both involve  
295 two fundamental elementary steps, radical addition and HAA, significant differences  
296 exist in their reactivity and pathway selectivity. In the radical addition pathway,  $\bullet\text{NO}_2$   
297 preferentially attacks the C3 site via transition state TS3\*. During this process, the  
298 forming C3–O bond length gradually shortens, ultimately leading to the formation of  
299 the nitrocyclohexadienyl radical intermediate IM3\*. This reaction mode resembles the



300 •OH-addition process suggesting some consistency in regioselectivity. However, HAA  
301 pathway displays markedly different behavior. Unlike •OH, which mainly abstracts hy-  
302 drogen atoms from the C5 site, •NO<sub>2</sub> preferentially abstracts the hydrogen atom of the  
303 hydroxyl group through transition state TS7\*. During this process, the breaking O–H  
304 bond is significantly elongated from 0.98 Å to 1.21 Å, while the newly formed H–ONO  
305 bond shortens from 1.08 Å to 0.97 Å.

306 This difference originates from the fundamentally different reaction characteristics  
307 of the two radicals. The high reactivity of •OH allows it to overcome unfavorable  
308 ground-state electrostatics and abstract the H atom at C5. By contrast, •NO<sub>2</sub> has much  
309 weaker electrophilicity and lower reactivity; its hydrogen abstraction depends on elec-  
310 trostatic complementarity and charge transfer, and it preferentially targets the hydroxyl  
311 hydrogen (Shenghur et al., 2014). Moreover, the •NO<sub>2</sub>-mediated hydrogen abstraction  
312 is often accompanied by substantial charge transfer, with a mechanism that more  
313 closely resembles proton-coupled electron transfer (PCET) (Tyburski et al., 2021). Thus,  
314 the O–H bond is more readily cleaved than a C–H bond, making the hydroxyl hydrogen  
315 the preferred abstraction site for •NO<sub>2</sub>.



316

317 **Figure 3** Thermodynamics, kinetics, and temperature dependence of the reactions of  
 318 2,4-DNP with O<sub>3</sub>, •OH, and •NO<sub>2</sub>. (a–c) reaction energy barriers (ΔE<sup>‡</sup>) and reaction  
 319 energies (Δ<sub>r</sub>E) for the key pathways (unit: kcal mol<sup>-1</sup>). (d–e) Temperature-dependent  
 320 reaction rate constants for the major channels.

321 The combined thermodynamic and kinetic analysis reveals that the reaction of O<sub>3</sub>  
 322 with 2,4-DNP is both thermodynamically favorable and kinetically accessible in the gas  
 323 and aqueous phases. As shown in Figure 3a, the most favorable gas-phase pathway, R6,  
 324 has a low energy barrier of 10.12 kcal mol<sup>-1</sup> and is strongly exothermic (ΔE = -35.56  
 325 kcal mol<sup>-1</sup>). In the aqueous phase, although the barrier increases moderately to 11.62  
 326 kcal mol<sup>-1</sup>, the reaction remains significantly exothermic. This indicates that solvation  
 327 does not fundamentally alter the thermodynamic driving force, and the relatively low  
 328 barrier ensures that the reaction remains kinetically feasible in both environmental me-  
 329 dia. In contrast, the reaction of 2,4-DNP with •OH shows even more favorable kinetics,  
 330 consistent with its role as the major atmospheric oxidant. The addition pathway in the



331 gas phase proceeds with an exceptionally low barrier of 2.84 kcal mol<sup>-1</sup>, substantially  
332 lower than the O<sub>3</sub>- initiated pathway, as presented in Figure 3b. The HAA pathway also  
333 presents a low barrier of 4.70 kcal mol<sup>-1</sup>. The similar barrier heights suggest that these  
334 two •OH-initiated pathways are kinetically competitive and are expected to occur con-  
335 currently under atmospheric conditions.

336 By comparison, the direct reaction of 2,4-DNP with •NO<sub>2</sub> is much less favorable.  
337 The overall process is endothermic and therefore non-spontaneous, as illustrated in Fig-  
338 ure 3c. Among the two plausible direct reaction pathways, radical addition to the aro-  
339 matic ring via the nitration pathway R3\* has a calculated energy barrier of 18.48 kcal  
340 mol<sup>-1</sup>, whereas HAA pathway has an even higher barrier of 41.39 kcal mol<sup>-1</sup>, making it  
341 far less accessible. Although the nitration channel is kinetically favored over HAA in  
342 the •NO<sub>2</sub> system, its energy barrier is still great higher than those of the corresponding  
343 •OH-initiated pathways and is also less thermodynamically favorable than both •OH-  
344 and O<sub>3</sub>-mediated reactions. Given these pronounced kinetic limitations, combined with  
345 the typically lower atmospheric concentration of •NO<sub>2</sub> relative to •OH and O<sub>3</sub>, the cal-  
346 culations strongly suggest that the direct transformation of 2,4-DNP initiated by •NO<sub>2</sub>  
347 is negligible under ambient atmospheric conditions (Shi et al., 2025; Chapleski et al.,  
348 2016). Therefore, the atmospheric degradation of 2,4-DNP is expected to be dominated  
349 by oxidation processes initiated by •OH radicals and O<sub>3</sub>. The possible involvement of  
350 •NO<sub>2</sub> in subsequent reactions with primary oxidation intermediates will be discussed  
351 separately to provide a complete mechanistic picture of its environmental fate.



352 This study further shows that the reaction behavior of 2,4-DNP in the aqueous  
353 phase differs markedly from that in gas phase and from that of simpler nitrophenol  
354 analogues. This difference is fundamentally attributed to the restructuring of molecular  
355 electronic distribution and reaction coordinates by the dynamic hydrogen-bonding net-  
356 work established between water and 2,4-DNP(Lyu et al., 2025). In contrast to the com-  
357 mon trend in which solvation stabilizes polar transition states and thus lowers energy  
358 barriers in mononitrophenols, 2,4-DNP exhibits the distinctive features of increased  
359 aqueous-phase energy barriers and solvent-induced switching of regioselectivity.

360 The increase in the aqueous-phase energy barriers can be attributed to the disrup-  
361 tive effect of the solvent on the intramolecular cooperativity inherent to 2,4-DNP. The  
362 simultaneous presence of a strongly electron-donating hydroxyl group and strongly  
363 electron-withdrawing nitro groups induces a pronounced intramolecular electric field,  
364 while the ortho-substitution geometry further enables stabilizing intramolecular hydro-  
365 gen bonds(Albinet et al., 2010). These structural features provide significant ground-  
366 state stabilization in the gas phase. In aqueous solution, water molecules compete with  
367 the internal hydrogen-bonding pattern by interacting with the polar functional groups,  
368 thereby partially disrupting the intramolecular hydrogen-bond network and weakening  
369 the internal electric field, which raises the ground-state energy(Yang et al., 2023a). Sol-  
370 vent reorganization also imposes an energetic penalty. Although solvation stabilizes the  
371 transition state, the net effect is an increase in the overall reaction barrier. The change  
372 in site selectivity likewise arises from solvent-mediated electron redistribution and



373 pathway switching. In the ring-addition pathway of  $\bullet\text{OH}$ , the C3 position is more fa-  
374 vorable in the gas phase because of the dominant conjugation effects. In the aqueous  
375 phase, however, water molecules enhance the local polarization near the hydroxyl-ad-  
376 jacent carbon C6, making another site more competitive for attack. For hydrogen ab-  
377 straction reactions, the gas-phase pathway is primarily governed by  $\sigma$  bond dissociation  
378 strength, where the C5–H bond is weakened by the adjacent nitro group and is therefore  
379 more susceptible to homolysis. In the aqueous phase, the mechanism shifts toward a  
380 PCET-like process. The hydroxyl hydrogen, due to its intrinsic acidity and the proton-  
381 transfer assistance provided by the hydrogen-bonding network of water, gains both ki-  
382 netic and thermodynamic advantages, becoming the dominant abstraction site in solu-  
383 tion.

384 Kinetic calculations further quantify the feasibility differences among various  
385 pathways under atmospheric conditions. To ensure physical significance and environ-  
386 mental interpretability, all rate constants were converted into the standard unit com-  
387 monly used in atmospheric chemistry ( $\text{cm}^3 \text{ molecule}^{-1} \text{ s}^{-1}$ ). Aqueous-phase data were  
388 converted from their original units of  $\text{M}^{-1} \text{ s}^{-1}$  using the Avogadro constant and vol-  
389 ume-unit conversion ( $1 \text{ M}^{-1} \text{ s}^{-1} = (1000/\text{NA}) \text{ cm}^3 \text{ molecule}^{-1} \text{ s}^{-1} \approx 1.66 \times 10^{-21} \text{ cm}^3 \text{ mol-}$   
390  $\text{ecule}^{-1} \text{ s}^{-1}$ ). As shown in Figure 3d–e, the rate constants of all major channels increase  
391 with temperature over the range of 200–400 K, exhibiting a characteristic Arrhe-  
392 nius-type temperature dependence. The total rate constants of the dominant pathways  
393 are listed in Table S2. Specifically, the  $\bullet\text{OH}$  pathway shows the highest kinetic activity,  
394 with total gas-phase and aqueous-phase rate constants of  $3.18 \times 10^{-15} \text{ cm}^3 \text{ molecule}^{-1} \text{ s}^{-1}$



395  $^1$  and  $2.25 \times 10^{-17} \text{ cm}^3 \text{ molecule}^{-1} \text{ s}^{-1}$ , respectively, at 298.15 K, further confirming its  
396 role as the dominant atmospheric oxidant. The  $\text{O}_3$  pathway also shows notable activity  
397 in the aqueous phase, with a total aqueous-phase rate constant of  $3.08 \times 10^{-17} \text{ cm}^3 \text{ mol-}$   
398  $\text{ecule}^{-1} \text{ s}^{-1}$ , highlighting the importance of aqueous environments in multiphase chem-  
399 istry. In contrast, the direct  $\bullet\text{NO}_2$  pathway exhibits extremely low kinetic activity, with  
400 total gas-phase and aqueous-phase rate constants as low as  $1.75 \times 10^{-28} \text{ cm}^3 \text{ molecule}^{-1}$   
401  $\text{s}^{-1}$  and  $3.93 \times 10^{-28} \text{ cm}^3 \text{ molecule}^{-1} \text{ s}^{-1}$ , respectively. These values are more than 13  
402 orders of magnitude lower than those of the  $\bullet\text{OH}$  pathway. Even under conditions of  
403 elevated  $\bullet\text{NO}_2$  concentration, the contribution of this pathway to the transformation of  
404 2,4-DNP is expected to be negligible. In summary, the atmospheric degradation of 2,4-  
405 DNP is kinetically dominated by  $\bullet\text{OH}$ , with  $\text{O}_3$  playing a significant role in the aqueous  
406 phase, while the direct transformation contribution of  $\bullet\text{NO}_2$  can be neglected in envi-  
407 ronmental assessments.

408

409

410

411

412

413

414

415

416



417 **Table 1** The experimental rate constant ( $\text{cm}^3 \text{ molecule}^{-1} \text{ s}^{-1}$ ) values of various phenols  
 418 with  $\text{O}_3$  in the gas phase.

| Compound        | Structure formula | Rate constants ( $\text{cm}^3 \text{ molecule}^{-1} \text{ s}^{-1}$ )    |
|-----------------|-------------------|--|
| 2,4-DNP         |                   | $4.23 \times 10^{-23}$   |
| 4-Nitrocatechol |                   | $1.48 \times 10^{-20}$ (Wang et al., 2026)                               |
| Nitrobenzene    |                   | $(7.00 \pm 0.20) \times 10^{-21}$ (Atkinson et al., 1987)                |
| Catechol        |                   | $(9.60 \pm 1.12) \times 10^{-18}$ (Sun et al., 2022; Tomas et al., 2003) |

419 This study establishes the reliability of the theoretically derived rate constant for  
 420 the reaction between 2,4-DNP and ozone through systematic benchmarking against  
 421 available experimental and computational data for structurally related aromatic com-  
 422 pounds. Although direct experimental measurements for this specific reaction are cur-  
 423 rently unavailable, as summarized in Table 1, the theoretical rate constant for the mo-  
 424 nonitro analogue nitrocatechol ( $1.48 \times 10^{-20} \text{ cm}^3 \text{ molecule}^{-1} \text{ s}^{-1}$ )(Wang et al., 2026) is  
 425 approximately three orders of magnitude lower than that of catechol(Sun et al., 2022;  
 426 Tomas et al., 2003), clearly demonstrating the strong inhibitory effect of the nitro group,  
 427 as an electron-withdrawing functional group on the ozone reactivity of the aromatic  
 428 ring. Building on this trend, the calculated rate constant for the dinitro compound 2,4-



429 DNP ( $4.23 \times 10^{-23} \text{ cm}^3 \text{ molecule}^{-1} \text{ s}^{-1}$ ) is reduced by an additional three orders of mag-  
430 nitude, quantitatively reflecting the cumulative electron-withdrawing effect of the two  
431 nitro substituents. This result is consistent with established activity trends of nitro-sub-  
432 stituted aromatic systems, thereby supporting the reasonableness of the calculated rate  
433 constant.

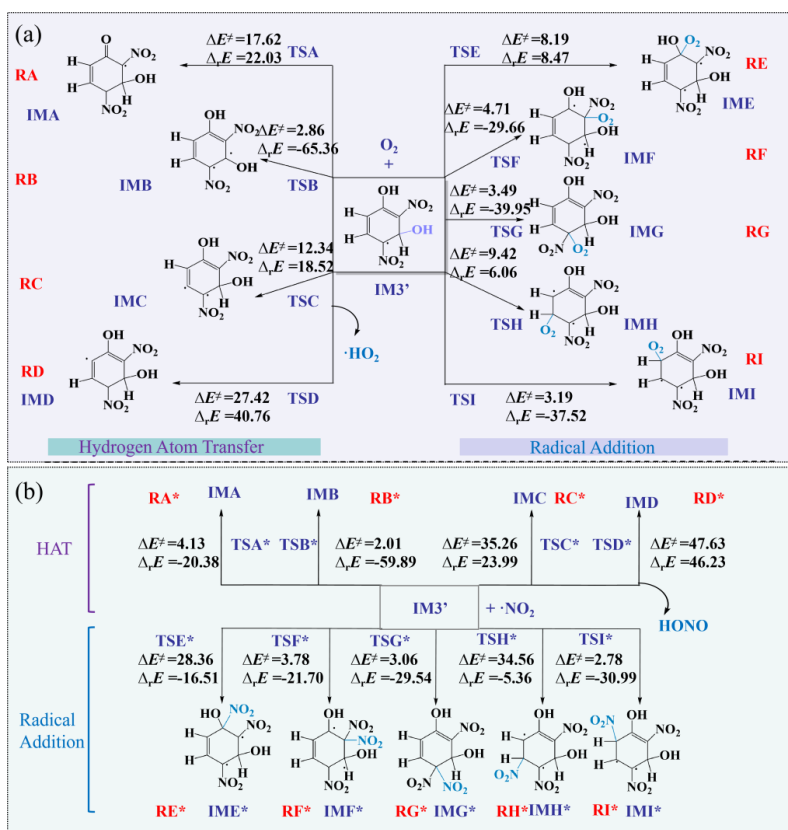
434 Furthermore, the predominance of substituent electronic effects in governing re-  
435 activity is independently corroborated. As detailed in Table S3, a systematic compari-  
436 son of the theoretical rate constants for the reaction of 2,4-DNP with  $\bullet\text{OH}$  with data for  
437 structural analogues demonstrates that the strong electron-withdrawing character of the  
438 nitro groups likewise controls the kinetics of this pathway. This consistency suggests  
439 that the electronic influence of nitro substituent is general across different oxidants ra-  
440 ther than being restricted to a single mechanism. Collectively, these results establish a  
441 robust and quantitatively consistent framework for predicting the atmospheric oxida-  
442 tion kinetics of aromatic pollutants on the basis of their fundamental electronic structure.

### 443 **3.1.3 The subsequent reactivity mechanism of the key intermediate IM3'**

444 As the primary initiator of atmospheric degradation of 2,4-DNP,  $\bullet\text{OH}$  generates  
445 the key radical intermediate IM3' via electrophilic addition. This highly reactive spe-  
446 cies can rapidly undergo secondary reactions with surrounding atmospheric constitu-  
447 ents. Reaction with molecular  $\text{O}_2$  typically governs its rapid oxidative evolution, while  
448 reaction with  $\bullet\text{NO}_2$  can lead to the formation of more toxic and more strongly light-ab-  
449 sorbing nitrated products. Therefore, to fully delineate the atmospheric transformation



450 pathways and final products of 2,4-DNP, it is essential to systematically investigate the  
 451 reaction mechanisms of IM3' with O<sub>2</sub> as well as •NO<sub>2</sub>.



452  
 453 **Figure 4** The subsequent reactivity mechanism of the key intermediate IM3' (unit: kcal  
 454 mol<sup>-1</sup>).

455 A systematic analysis was conducted for the reaction pathways of the intermediate  
 456 IM3' with O<sub>2</sub> and •NO<sub>2</sub>. For the reaction with O<sub>2</sub>, as shown in Figure 4a, IM3' prime  
 457 mainly evolves through two competing pathways, namely HAA and radical addition.  
 458 The HAA pathway contains four distinct subchannels, among which the RB channel is  
 459 the most favorable both thermodynamics and kinetics. It is characterized by a remark-



ably low transition-state energy barrier of  $2.86 \text{ kcal mol}^{-1}$  and a highly exothermic reaction energy of  $-65.36 \text{ kcal mol}^{-1}$ . In this process, the  $\text{O}_2$  molecule approaches the activated C3–H bond. The reaction is directed to the C3 position because this carbon is flanked by two strongly electron-withdrawing nitro groups at the adjacent C2 and C4 positions. This electronic effect substantially lowers the electron density and weakens the C3–H bond, making it the most favorable site for hydrogen abstraction. Key structural parameters in transition state TSB reveal a concerted mechanism: the distance between the attacking oxygen atom  $\text{O}_a$  of  $\text{O}_2$  and the transferring hydrogen shortens to approximately  $1.17 \text{ \AA}$ , while the breaking C3–H bond elongates to about  $1.30 \text{ \AA}$ . This synchronous bond-breaking and bond-forming process yields the phenoxy radical intermediate IMB and the hydroperoxyl radical ( $\bullet\text{HO}_2$ ). In contrast, the other HAA channels involving abstraction from the C5, C6, or hydroxyl positions have much higher energy barriers and are therefore kinetically uncompetitive under realistic atmospheric conditions. In the competing radical addition pathway, the most favorable channel is RI, in which  $\text{O}_2$  adds to the relatively electron-rich C4 position via the transition state TSI. This process has an energy barrier of  $3.19 \text{ kcal mol}^{-1}$  and is exothermic by  $-37.52 \text{ kcal mol}^{-1}$ . Because this barrier is close to that of the optimal HAA channel RB, the HAA and radical addition pathways for the reaction of IM3' with  $\text{O}_2$  are expected to compete directly at the molecular level.

The reaction of IM3' with  $\bullet\text{NO}_2$  similarly follows a competitive mechanism involving HAA and radical addition (Figure 4b). Within the HAA pathway, the RB\* channel shows a clear advantage analogous similar to that observed in the  $\text{O}_2$  system,



482 with a low energy barrier of  $2.01 \text{ kcal mol}^{-1}$  and a highly exothermic reaction energy of  
483  $-59.89 \text{ kcal mol}^{-1}$ . The mechanism of this process is highly consistent with that of the  
484  $\text{O}_2$ -involved RB channel, which both involve the oxidant abstracting the hydrogen atom  
485 from the C3 position, yielding the identical phenoxy radical intermediate IMB, while  
486 producing HONO or  $\bullet\text{HO}_2$ , respectively. In the radical addition pathway, the most fea-  
487 sible route is the channel  $\text{RI}^*$ , with a barrier of  $2.78 \text{ kcal mol}^{-1}$  and a reaction energy of  
488  $-30.99 \text{ kcal mol}^{-1}$ . Similar to the  $\text{O}_2$  addition pathway,  $\bullet\text{NO}_2$  preferentially adds to the  
489 relatively electron-dense C4 position, generating the nitro-substituted cyclohexadienyl  
490 radical intermediate  $\text{IMI}^*$ . Comparison of the lowest energy barriers for the two path-  
491 ways reveals that the HAA path is kinetically and slightly more favorable than the rad-  
492 ical addition path. This establishes the HAA mechanism as the dominant mechanism in  
493 the reaction of  $\text{IM3}'$  with  $\bullet\text{NO}_2$ , consistent with the conclusion drawn for the  $\text{O}_2$  system.

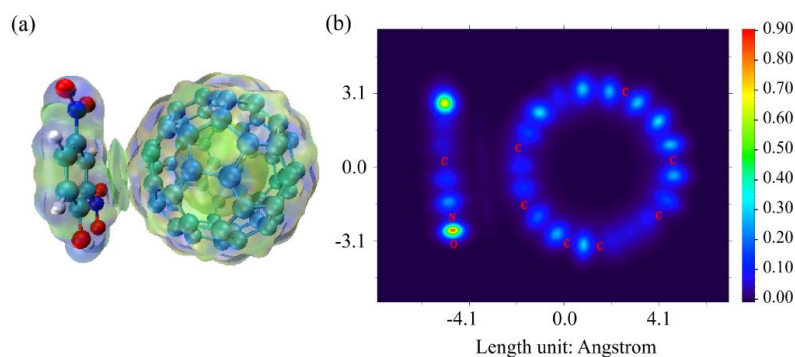
494 The above computational results elucidate, at the microscopic mechanistic level,  
495 the possible pathways of  $\text{IM3}'$  with  $\text{O}_2$  and  $\bullet\text{NO}_2$ . However, to assess its ultimate fate  
496 in the real atmospheric, it is necessary to further consider the competition between these  
497 oxidants under realistic atmospheric concentrations. In particular, the large concentra-  
498 tion difference between  $\text{O}_2$  and  $\bullet\text{NO}_2$  must be taken into account when evaluating the  
499 dominant degradation channels and their environmental significance.

### 500 **3.2. Molecular dynamics**

501 Although the homogeneous oxidation mechanisms of 2,4-DNP in the gas and  
502 aqueous phases have been clarified, its heterogeneous interfacial behavior on aerosol  
503 particle surfaces remains to be elucidated. As a representative model of atmospheric



504 nanoparticles, C60 offers an ideal system for probing the non-covalent interactions be-  
505 tween pollutants and particulate matter, owing to its well-defined carbon framework  
506 and surface curvature (Athar and Patnaik, 2022). In this study, the IGM was employed  
507 to qualitatively and quantitatively analyze the weak interactions within the adsorption  
508 complexes (Lu and Chen, 2022), thereby revealing the interactions that govern the in-  
509 terfacial behavior at the molecular level.



510

511 **Figure 5** IGM analysis of intermolecular interactions in the 2,4-DNP-C60 aggregate.

512 (a) three-dimensional (3D) IGM isosurface map. (b) Two-dimensional (2D) IGM den-

513 sity map.

514 The intermolecular interactions within the 2,4-DNP-C60 aggregate were charac-

515 terized utilizing the Independent Gradient Model by defining each monomer as an in-

516 dividual fragment. The intermolecular interaction pattern at the 2,4-DNP-C60 interface

517 is elucidated jointly by the three-dimensional IGM isosurface map (Figure 5a) and the

518 two-dimensional density map (Figure 5b), which exhibit excellent consistency. Accord-

519 ing to the principles of IGM analysis, the green and light-green isosurface regions,



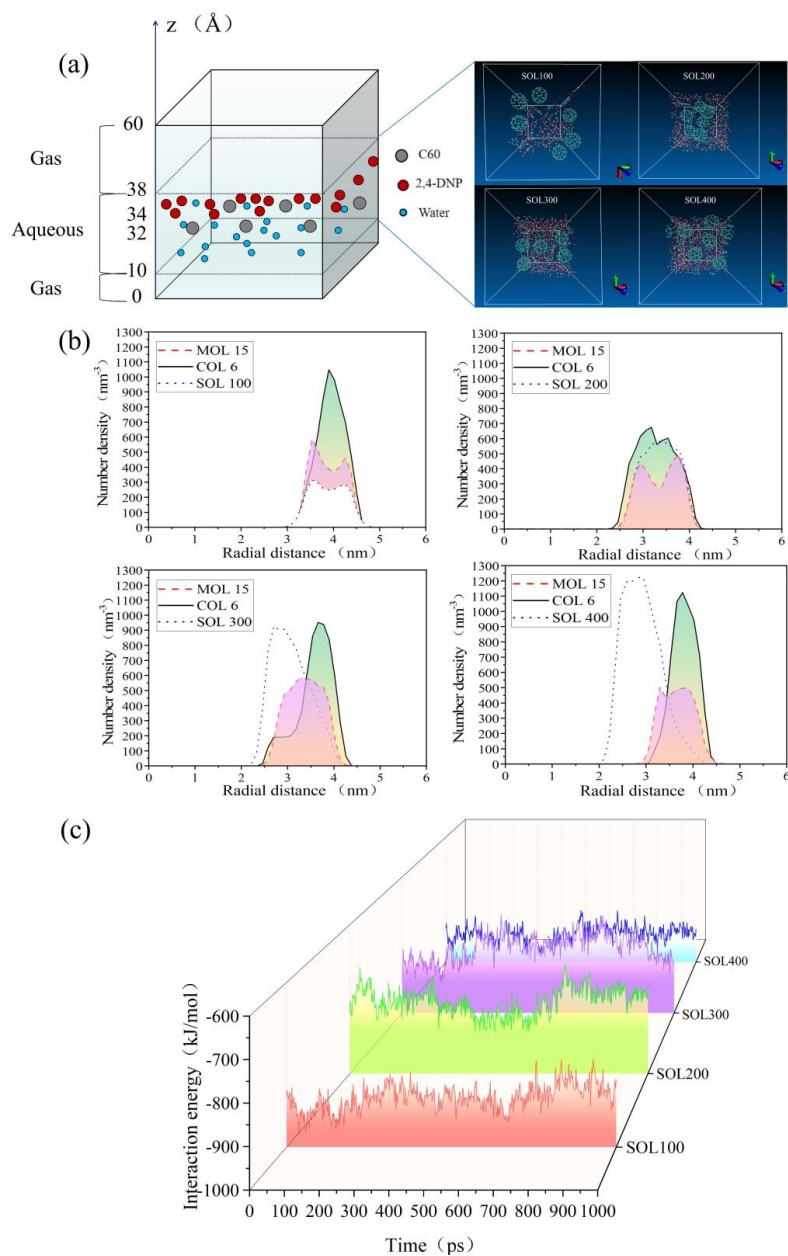
520 where  $\text{sign}(\lambda_2) \approx 0$ , correspond to van der Waals (vdW) interactions, indicative of dif-  
521 fuse and non-directional weak attractions. In contrast, the blue regions, characterized  
522 by  $\text{sign}(\lambda_2) < 0$ , indicate directional interactions such as hydrogen bonds or strong elec-  
523 trostatic attractions, which are associated with more localized electron-density distribu-  
524 tions.

525 Specifically, the extensive green/light-green isosurface between the C60 cage and  
526 the benzene ring of 2,4-DNP corresponds closely to the continuous blue-to-light-blue  
527 signal band in the 2D density map ( $\delta g_{\text{inter}} \approx 0.10\text{--}0.30$ ), confirming that vdW interac-  
528 tions, mainly dispersion and induction forces arising from the  $\pi$ -electron clouds of the  
529 benzene ring and fullerene surface, dominant the interfacial binding between 2,4-DNP  
530 and C60. Meanwhile, distinct blue regions are observed near the polar functional groups  
531 of 2,4-DNP, namely the nitro and hydroxyl moieties. These features manifest as local-  
532 ized yellow-green hotspots in the 2D density map ( $\delta g_{\text{inter}} \approx 0.60\text{--}0.80$ ), indicating  
533 stronger polar interactions. These interactions can be attributed to specific directional  
534 forces, including a C–H $\cdots\pi$  hydrogen bond involving the hydrogen atom of the –OH  
535 group and the delocalized  $\pi$ -electron cloud of C60, as well as a dipole- $\pi$  interaction  
536 between the oxygen atoms of the –NO<sub>2</sub> groups and the fullerene surface. These syner-  
537 gistic polar interactions enhance both the binding selectivity and the overall stability of  
538 the 2,4-DNP-C60 interface.

539 Further analysis indicates that the 2,4-DNP molecule preferentially adsorbs with  
540 its benzene ring approximately parallel to the C60 surface. In this configuration, the



541 nonpolar benzene ring maximizes the dispersion interaction area by closely approach-  
542 ing the carbon cage via vdW forces, while the polar –OH and –NO<sub>2</sub> groups remain  
543 oriented outward. This arrangement not only avoids steric repulsion with the C<sub>60</sub> sur-  
544 face corresponding to strong steric hindrance, but also facilitates hydrogen-bond-net-  
545 work formation between the polar groups of neighboring 2,4-DNP molecules. In the  
546 2D IGM cross-sectional map, this orientation is reflected by a clear spatial separation  
547 between the polar hotspots of the 2,4-DNP and the van der Waals signal band associated  
548 with C<sub>60</sub>, with the hotspot positions precisely corresponding to the atomic coordinates  
549 of the polar functional groups.



550

551 **Figure 6** (a) Molecular dynamics simulation framework construction (MOL: 2,4-DNP;

552 COL: C60; SOL: water). (b) z-axis number density profile of molecules (units: nm<sup>-3</sup>).

553 (c) Hydration-dependent adsorption energies of 2,4-DNP on C60 (units: kJ mol<sup>-1</sup>).



554 Building upon the fundamental interaction mechanisms revealed by IGM in the  
555 anhydrous system, molecular dynamics simulations were further carried out to how hy-  
556 dration, as a key environmental factor, dynamically regulates the adsorption behavior  
557 of 2,4-DNP on C60 under atmospherically relevant conditions. Figure 6a illustrates the  
558 initial simulation setup, which consists of 15 molecules of 2,4-DNP and 6 molecules of  
559 C60 placed in a three-layer simulation box measuring  $30 \times 30 \times 60 \text{ \AA}^3$ , with a gas-aque-  
560 ous-gas sandwich structure. Different hydration levels were modeled by varying the  
561 number of water molecules from SOL100 to SOL400. The system then underwent en-  
562 ergy minimization and molecular dynamics relaxation to obtain an equilibrated struc-  
563 ture. In the aqueous phase, the distribution of 2,4-DNP and C60 gradually shifted to-  
564 ward the center of the water layer as the number of water molecules increased, indicat-  
565 ing that the introduction of water significantly altered the spatial distribution pattern of  
566 the solutes.

567 The number-density distribution profiles along the z-axis in Figure 6b further re-  
568 veal the influence of hydration on the axial distribution and aggregation behavior of the  
569 solute molecules. Combined with the strong intermolecular interactions revealed by  
570 IGM in the anhydrous system, it can be inferred that under low hydration conditions,  
571 2,4-DNP and C60 tend to form compact aggregates because of their relatively strong  
572 mutual attraction. As the number of water molecules increases from SOL200 to  
573 SOL400, the density peak shifts toward larger radial distances (4.0–4.5 nm) and its  
574 height gradually rises. This indicates that water molecules disrupt the close aggregation  
575 tendency between 2,4-DNP and C60 through steric hindrance effects, promoting the



576 outward diffusion of solute molecules along the z-axis and thereby significantly en-  
577 hancing the overall dispersity of the system.

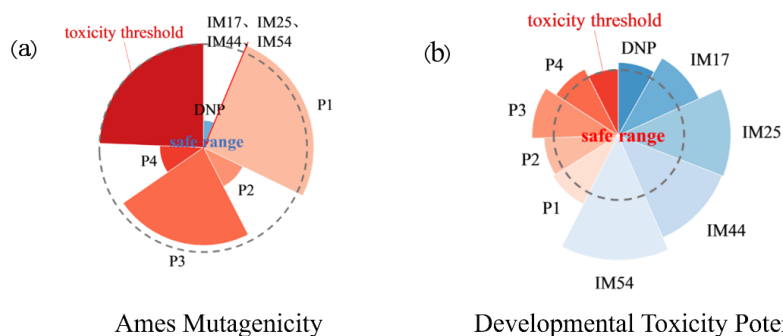
578       Based on the temporal evolution of the interaction energies shown in Figure 6c,  
579 the dynamic regulatory role of hydration on intermolecular adsorption behavior can be  
580 further interpreted from an energetic perspective. In the low-hydration system SOL100,  
581 the interaction energy remains stable at approximately  $-850 \text{ kJ mol}^{-1}$ . Its relatively large  
582 negative value is consistent with the compact aggregated state shown in Figure 6b, in-  
583 dicating strong direct adsorption between 2,4-DNP and C60 under these conditions. As  
584 the number of water molecules increases to SOL200, the absolute value of the interac-  
585 tion energy increases further, suggesting enhanced intermolecular attraction. This  
586 change may originate from moderate hydration, where water molecules promote spe-  
587 cific orientations and stabilize solute interactions through effects such as dielectric  
588 screening or indirect bridging(Lyu et al., 2025). However, when the hydration level  
589 further increases to SOL400, the absolute value of the interaction energy decreases,  
590 implying a significant weakening of intermolecular adsorption. This indicates that un-  
591 der high hydration conditions, water molecules suppress the direct interaction between  
592 2,4-DNP and C60, thereby driving the system toward a more dispersed and stable solv-  
593 ated state. This non-monotonic energy trend, which first strengthens and then weakens,  
594 is consistent with the morphological evolution of solute distribution shown in Figure  
595 6b, namely a transition from an initially aggregated state to a more dispersed one. To-  
596 gether, these results reveal the complex regulatory role of hydration in interfacial ad-  
597 sorption behavior.



598 To assess statistical uncertainty arising from initial conditions, four independent  
599 replica simulations were performed for each hydration level by assigning distinct initial  
600 atomic velocities, thereby generating statistically independent trajectories in phase  
601 space. Error analysis demonstrates that the main conclusions regarding the adsorption  
602 configuration and distribution of 2,4-DNP at the gas-aqueous interface remain con-  
603 sistent across all replicas, underscoring the robustness and reproducibility of the results.

### 604 **3.3 Ecotoxicity assessment**

605 The reaction of ozone with aromatic rings follows a relatively well-defined mech-  
606 anism and produces a comparatively clear product spectrum, making it a comparatively  
607 model for evaluating the directional impact of atmospheric oxidation on the toxicity of  
608 2,4-DNP. By focusing on O<sub>3</sub>, the oxidant with of high environmental relevance, this  
609 study enables a precise analysis of the oxidation degradation pathways of 2,4-DNP and  
610 the toxicity of its products. The conclusions drawn here can provide a crucial toxico-  
611 logical reference for future investigations of the more complex atmospheric oxidation  
612 networks involving radicals such as •OH and •NO<sub>2</sub>. Accordingly, based on the key in-  
613 termediates and final products (IM17, IM25, IM44, IM54, P1–P4) identified in Figure  
614 S2, their mutagenic and developmental toxicity potentials were predicted using the  
615 T.E.S.T. tool(Epa, 2020), aiming to reveal the toxicity evolution pattern along this spe-  
616 cific oxidation process.



617 Ames Mutagenicity Developmental Toxicity Potential  
618 **Figure 7** Toxicity prediction of 2,4-DNP and its transformation products. (a) Ames  
619 mutagenicity. (b) Developmental toxicity.

620 The risk differences in Ames mutagenicity and developmental toxicity potential  
621 between 2,4-DNP and the intermediates (IMs series) and final products (Ps series) gen-  
622 erated from its reaction with ozone are intuitively illustrated in Figure 7. Regarding  
623 Ames mutagenicity in Figure 7a, the parent compound 2,4-DNP exhibits a predicted  
624 value of 0.13 that falls within the safety threshold. The specific data are presented in  
625 Table S4. In contrast, its ozonolysis products display a marked divergence in mutagenic  
626 potential. Although primary intermediates (IM17, IM25, IM44, IM54) show no detect-  
627 able mutagenicity, the final products generally demonstrate elevated mutagenic risk.  
628 Notably, the predicted value for product P1 (0.53) exceeds the toxicity threshold, plac-  
629 ing it within the high-risk zone. This result clearly indicates that the ozonolysis does  
630 not necessarily reduce the mutagenicity of 2,4-DNP, instead, by generating more reac-  
631 tive intermediates and final products, it may significantly increase the overall genotoxic  
632 risk of the reaction system.

633 In terms of developmental toxicity in Figure 7b, 2,4-DNP itself shows a baseline  
634 potential of 0.55, which is further exacerbated by ozonolysis. All derived products show



635 higher developmental toxicity than the parent compound, with the risk reaching a max-  
636 imum for IM54 (0.94). Notably, P2 and P4, despite their relatively low Ames mutagen-  
637 icity (0.21), still exhibit a developmental toxicity potential of 0.56, which are higher  
638 than that of the parent compound. This reveals a decoupling between mutagenicity and  
639 developmental toxicity, suggesting that the oxidation process may generate novel haz-  
640 ardous specific developmental toxicity even when their mutagenic potential remains  
641 relatively low. Overall, the analysis indicates that the ozonolysis of 2,4-DNP does not  
642 constitute a harmless degradation pathway. On the contrary, it leads to the generation  
643 of more intermediate and final products with enhanced mutagenic and developmental  
644 toxicity.

645 The QSAR models utilized in this study provide valuable preliminary information  
646 for risk prioritization, the inherent uncertainties associated with *in silico* predictions  
647 must be acknowledged. The predictive performance is fundamentally constrained by  
648 the chemical space of the training sets and the defined applicability domains. For struc-  
649 turally distinct species such as 2,4-DNP and its various derivatives, the confidence lev-  
650 els of the predictions may be diminished because these models cannot fully elucidate  
651 specific toxicological modes of action. In addition, categorical predictions with proba-  
652 bility scores close to threshold are inherently unstable, suggesting that the “not detected”  
653 Ames mutagenicity signals for intermediates such as IM17, IM25, IM44, and IM54  
654 may reflect model limitations rather than a definitive absence of toxicity. These com-  
655 pounds should therefore be regarded as high-priority targets for experimental validation.  
656 Furthermore, these computational frameworks necessarily simplify complex biological



657 endpoints such as developmental toxicity. Therefore, the present findings should be  
658 interpreted as hypothesis-generating rather than definitive. Future studies are recom-  
659 mended to validate these predictions through in vitro Ames tests and zebrafish embryo  
660 development experiments, and to develop targeted removal strategies for toxic nitro-  
661 carbonyl-type products.

#### 662 **4 Conclusion**

663 This study systematically investigated the chemical transformation mechanisms,  
664 multiphase interfacial behavior, and toxicity evolution of 2,4-DNP in the atmosphere  
665 using an integrated computational framework combining DFT, MD simulations, and  
666 QSAR models. The main quantitative findings are: the atmospheric degradation of 2,4-  
667 DNP is dominated by  $\bullet\text{OH}$  and  $\text{O}_3$  oxidation pathways, while direct reaction with  $\bullet\text{NO}_2$   
668 is kinetically unfavorable (gas-phase rate constant  $\sim 10^{-28} \text{ cm}^3 \text{ molecule}^{-1} \text{ s}^{-1}$ , more than  
669 13 orders of magnitude lower than that of  $\bullet\text{OH}$ ); solvation effects and the electron-with-  
670 drawing nitro groups suppress the initial reaction rates; the key radical intermediate  
671 from  $\bullet\text{OH}$  addition reacts with  $\text{O}_2$  and  $\bullet\text{NO}_2$  predominantly via HAA; MD simulations  
672 reveal that the adsorption behavior of 2,4-DNP on atmospheric particle surrogates is  
673 regulated non-monotonically by the degree of interfacial hydration. Under low-hydra-  
674 tion conditions, solute-particle interactions are enhanced, while under high-hydration  
675 conditions, adsorption is weakened due to competitive binding and steric hindrance ef-  
676 fects from water molecules; and ozonolysis of 2,4-DNP does not lead to harmless deg-  
677 radation but generates secondary products with significantly increased mutagenicity  
678 and developmental toxicity. Collectively, 2,4-DNP is a relatively persistent pollutant



679 whose atmospheric lifetime depends strongly on humidity and whose oxidation does  
680 not detoxify but rather amplifies environmental risk. Compared to previous studies that  
681 focused on gas-phase photolysis and assumed oxidative detoxification, our work quan-  
682 tifies the cumulative electron-withdrawing effect of two nitro groups (rate constant  
683 three orders lower than mononitrocatechol) and reveals that ozonolysis increases tox-  
684 icity, challenging conventional assumptions.

685 Several limitations should be noted: the aerosol surrogate (C60) and QSAR tox-  
686 icity models do not fully capture real atmospheric particle complexity or definitive tox-  
687 icological outcomes; experimental validation via *in vitro* and *in vivo* assays is needed.  
688 Despite these caveats, our findings have clear implications for atmospheric chemistry  
689 and climate. The humidity-dependent adsorption behavior implies that 2,4-DNP may  
690 have longer residence time and greater long-range transport under dry conditions, af-  
691 fecting its global distribution. Moreover, the production of toxic transformation prod-  
692 ucts suggests that current air quality models may underestimate the health risks of ni-  
693 trophenolic emissions. Regulatory attention to 2,4-DNP and its derivatives is therefore  
694 warranted.

#### 695 **Data availability**

696 The data supporting this article have been included as part of the supplementary  
697 information or are available upon request.

#### 698 **Author contributions**

699 Chenlei Wang conceptualized the study, curated the data, validated the results, and  
700 wrote the original draft. Ran Li and Jiaying Sun conceptualized the study and curated



701 the data. Zihan Zhang curated the data. Nan Zhao developed the software and validated  
702 the results. Zuju Ma developed the software, performed the visualization, and carried  
703 out the investigation. Maoxia He developed the methodology, performed the visualiza-  
704 tion, and carried out the investigation. Leilei Liu reviewed and edited the manuscript  
705 and acquired the funding. Jianfei Sun curated the data, reviewed and edited the manu-  
706 script, acquired the funding, supervised the project, and administered the project.

#### 707 **Competing interests**

708 The authors declare that they have no conflict of interest.

#### 709 **Acknowledgements**

710 This work was financially supported by Shandong Provincial Natural Science  
711 Foundation ZR2024MB037, and Natural Science Foundation of Yantai 2024JCYJ065.

#### 712 **References**

713 Ahmaruzzaman, M., Mishra, S. R., Gadore, V., Yadav, G., Roy, S., Bhattacharjee, B.,  
714 Bhuyan, A., Hazarika, B., Darabdhara, J., and Kumari, K.: Phenolic compounds in wa-  
715 ter: From toxicity and source to sustainable solutions - An integrated review of removal  
716 methods, advanced technologies, cost analysis, and future prospects, *Journal of Envi-  
717 ronmental Chemical Engineering*, 12, 10.1016/j.jece.2024.112964, 2024.

718 Albinet, A., Minero, C., and Vione, D.: Phototransformation processes of 2,4-dinitro-  
719 phenol, relevant to atmospheric water droplets, *Chemosphere*, 80, 753-758,  
720 10.1016/j.chemosphere.2010.05.016, 2010.

721 Athar, M. and Patnaik, A.: Through-Bond-Driven Through-Space Interactions in a Full-  
722 erene C<sub>60</sub> Noncovalent Dyad: An Unusual Strong Binding between Spherical and Pla-  
723 nar  $\pi$  Electron Clouds and Culmination of Dyadic Fractals, *Journal of Physical Chem-  
724 istry A*, 126, 3629-3641, 10.1021/acs.jpca.1c10828, 2022.

725 Atkinson, R., Tuazon, E. C., Wallington, T. J., Aschmann, S. M., Arey, J., Winer, A. M.,  
726 and Pitts, J. N.: Atmospheric chemistry of aniline, N,N-dimethylaniline, pyridine, 1,3,5-



- 727 triazine, and nitrobenzene, *Environmental Science & Technology*, 21, 64-72,  
728 10.1021/es00155a007, 1987.
- 729 Barton, D. H. R. and Cookson, R. C.: The Principles of Conformational Analysis, *Quarterly Reviews*, 10, 44-82, 10.1039/qr9561000044, 1956.
- 731 Benfenati, E., Benigni, R., DeMarini, D. M., Helma, C., Kirkland, D., Martin, T. M.,  
732 Mazzatorta, P., Ouédraogo-Arras, G., Richard, A. M., Schilter, B., Schoonen, W.,  
733 Snyder, R., and Yang, C.: Predictive Models for Carcinogenicity and Mutagenicity:  
734 Frameworks, State-of-the-Art, and Perspectives, *Journal of Environmental Science and*  
735 *Health Part C-Environmental Carcinogenesis & Ecotoxicology Reviews*, 27, 57-90,  
736 10.1080/10590500902885593, 2009.
- 737 Canneaux, S., Bohr, F., and Henon, E.: KiSTheLP: A Program to Predict Thermody-  
738 namic Properties and Rate Constants from Quantum Chemistry Results, *Journal of*  
739 *Computational Chemistry*, 35, 82-93, 10.1002/jcc.23470, 2014.
- 740 Cassano, A., Manganaro, A., Martin, T., Young, D., Piclin, N., Pintore, M., Bigoni, D.,  
741 and Benfenati, E.: CAESAR models for developmental toxicity, *Chemistry Central*  
742 *Journal*, 4, 10.1186/1752-153x-4-s1-s4, 2010.
- 743 Chapleski, R. C., Zhang, Y. F., Troya, D., and Morris, J. R.: Heterogeneous chemistry  
744 and reaction dynamics of the atmospheric oxidants, O<sub>3</sub>, NO<sub>3</sub>, and OH, on organic sur-  
745 faces, *Chemical Society Reviews*, 45, 3731-3746, 10.1039/c5cs00375j, 2016.
- 746 Delaria, E. R. and Cohen, R. C.: Measurements of Atmosphere-Biosphere Exchange of  
747 Oxidized Nitrogen and Implications for the Chemistry of Atmospheric NO<sub>x</sub>, *Accounts*  
748 *of Chemical Research*, 56, 1720-1730, 10.1021/acs.accounts.3c00090, 2023.
- 749 EPA, U. S.: User's Guide for T.E.S.T. (version 5.1) (Toxicity Estimation Software Tool):  
750 A Program to Estimate Toxicity from Molecular Structure., U.S. Environmental Pro-  
751 tection Agency, 2020.
- 752 Fan, W. L., Chen, T., Zhu, Z. L., Zhang, H., Qiu, Y. L., and Yin, D. Q.: A review of  
753 secondary organic aerosols formation focusing on organosulfates and organic nitrates,  
754 *Journal of Hazardous Materials*, 430, 10.1016/j.jhazmat.2022.128406, 2022.
- 755 Frisch, M. J., Trucks, G. W., Schlegel, H. B., Scuseria, G. E., Robb, M. A., Cheeseman,  
756 J. R., Scalmani, G., Barone, V., Petersson, G. A., Nakatsuji, H., Li, X., Caricato, M.,



757 Marenich, A. V., Bloino, J., Janesko, B. G., Gomperts, R., Mennucci, B., Hratchian, H.  
758 P., Ortiz, J. V., Izmaylov, A. F., Sonnenberg, J. L., Williams, Ding, F., Lipparini, F.,  
759 Egidi, F., Goings, J., Peng, B., Petrone, A., Henderson, T., Ranasinghe, D., Zakrzewski,  
760 V. G., Gao, J., Rega, N., Zheng, G., Liang, W., Hada, M., Ehara, M., Toyota, K., Fukuda,  
761 R., Hasegawa, J., Ishida, M., Nakajima, T., Honda, Y., Kitao, O., Nakai, H., Vreven, T.,  
762 Throssell, K., Montgomery Jr., J. A., Peralta, J. E., Ogliaro, F., Bearpark, M. J., Heyd,  
763 J. J., Brothers, E. N., Kudin, K. N., Staroverov, V. N., Keith, T. A., Kobayashi, R., Nor-  
764 mand, J., Raghavachari, K., Rendell, A. P., Burant, J. C., Iyengar, S. S., Tomasi, J.,  
765 Cossi, M., Millam, J. M., Klene, M., Adamo, C., Cammi, R., Ochterski, J. W., Martin,  
766 R. L., Morokuma, K., Farkas, O., Foresman, J. B., and Fox, D. J.: Gaussian 16 Rev.  
767 C.01, 2016.

768 Grundlingh, J., Dargan, P. I., El-Zanfaly, M., and Wood, D. M.: 2,4-dinitrophenol  
769 (DNP): a weight loss agent with significant acute toxicity and risk of death, *J Med*  
770 *Toxicol*, 7, 205-212, [10.1007/s13181-011-0162-6](https://doi.org/10.1007/s13181-011-0162-6), 2011.

771 Hu, W., Liu, D. D., Su, S. H., Ren, L. J., Ren, H., Wei, L. F., Yue, S. Y., Xie, Q. R.,  
772 Zhang, Z. M., Wang, Z. H., Yang, N., Wu, L. B., Deng, J. J., Qi, Y. L., and Fu, P. Q.:  
773 Photochemical Degradation of Organic Matter in the Atmosphere, *Advanced Sustaina-*  
774 *ble Systems*, 5, [10.1002/adsu.202100027](https://doi.org/10.1002/adsu.202100027), 2021.

775 Humphrey, W., Dalke, A., and Schulten, K.: VMD: Visual molecular dynamics, *Journal*  
776 *of Molecular Graphics*, 14, 33-38, [https://doi.org/10.1016/0263-7855\(96\)00018-5](https://doi.org/10.1016/0263-7855(96)00018-5),  
777 1996.

778 Kroll, J. H. and Seinfeld, J. H.: Chemistry of secondary organic aerosol: Formation and  
779 evolution of low-volatility organics in the atmosphere, *Atmospheric Environment*, 42,  
780 3593-3624, [10.1016/j.atmosenv.2008.01.003](https://doi.org/10.1016/j.atmosenv.2008.01.003), 2008.

781 Kromann, J. C., Steinmann, C., and Jensen, J. H.: Improving solvation energy predic-  
782 tions using the SMD solvation method and semiempirical electronic structure methods,  
783 *Journal of Chemical Physics*, 149, [10.1063/1.5047273](https://doi.org/10.1063/1.5047273), 2018.

784 Lee, D., Schwegler, E., and Kanai, Y.: Dependence of Water Dynamics on Molecular  
785 Adsorbates near Hydrophobic Surfaces: First-Principles Molecular Dynamics Study,  
786 *Journal of Physical Chemistry C*, 118, 8508-8513, [10.1021/jp502850k](https://doi.org/10.1021/jp502850k), 2014.



- 787 Lefebvre, C., Rubez, G., Khartabil, H., Boisson, J. C., Contreras-García, J., and Hénon,  
788 E.: Accurately extracting the signature of intermolecular interactions present in the NCI  
789 plot of the reduced density gradient versus electron density, *Physical Chemistry Chem-*  
790 *ical Physics*, 19, 17928-17936, 10.1039/c7cp02110k, 2017.
- 791 Li, J., Han, Z. W., Sun, Y. L., Li, J. W., and Liang, L.: Chemical formation pathways of  
792 secondary organic aerosols in the Beijing-Tianjin-Hebei region in wintertime, *Atmos-*  
793 *pheric Environment*, 244, 10.1016/j.atmosenv.2020.117996, 2021.
- 794 Li, J., Han, Z. W., Wu, J., Tao, J., Li, J. W., Sun, Y. L., Liang, L., Liang, M. J., and Wang,  
795 Q. G.: Secondary organic aerosol formation and source contributions over east China  
796 in summertime, *Environmental Pollution*, 306, 10.1016/j.envpol.2022.119383, 2022a.
- 797 Li, M., Wang, X. F., Lu, C. Y., Li, R., Zhang, J., Dong, S. W., Yang, L. X., Xue, L. K.,  
798 Chen, J. M., and Wang, W. X.: Nitrated phenols and the phenolic precursors in the at-  
799 mosphere in urban Jinan, China, *Science of the Total Environment*, 714, 10.1016/j.sci-  
800 *totenv.2020.136760*, 2020.
- 801 Li, M., Wang, X. F., Zhao, Y. N., Du, P., Li, H. Y., Li, J. R., Shen, H. Q., Liu, Z. Y.,  
802 Jiang, Y. R., Chen, J., Bi, Y. J., Zhao, Y., Xue, L. K., Wang, Y., Chen, J. M., and Wang,  
803 W. X.: Atmospheric Nitrated Phenolic Compounds in Particle, Gaseous, and Aqueous  
804 Phases During Cloud Events at a Mountain Site in North China: Distribution Charac-  
805 teristics and Aqueous-Phase Formation, *Journal of Geophysical Research-Atmospheres*,  
806 127, 10.1029/2022jd037130, 2022b.
- 807 Li, P. Y., Feng, L., Li, G. Y., and Bai, F. Q.: Effects of Electron Donating Ability of  
808 Substituents and Molecular Conjugation on the Electronic Structures of Organic Radi-  
809 cals, *Chemical Research in Chinese Universities*, 39, 202-207, 10.1007/s40242-023-  
810 2364-2, 2023.
- 811 Liu, X. H., Meng, T. T., Bai, F. Y., Ni, S., and Zhao, Z.: Theoretical investigation on the  
812 atmospheric degradation mechanism, kinetics, and fate of hydroxymethyl nitrate initi-  
813 ated by OH radicals, *New Journal of Chemistry*, 47, 11414-11424, 10.1039/d3nj01628e,  
814 2023.
- 815 Liu, Z. Y. and Lu, T.: Theoretical Insight into Complexation Between Cyclocarbons and  
816 C60 Fullerene, *Chemistry-a European Journal*, 30, 10.1002/chem.202402227, 2024.



- 817 Lu, T., TST calculator, <http://sobereva.com/310> (accessed 12 11, 2025).
- 818 Lu, T., Sobtop, Version [1.0], <http://sobereva.com/soft/Sobtop> (accessed on 17 01 2026).
- 819 Lu, T. and Chen, F. W.: Multiwfn: A multifunctional wavefunction analyzer, *Journal of*  
820 *Computational Chemistry*, 33, 580-592, 10.1002/jcc.22885, 2012.
- 821 Lu, T. and Chen, Q. X.: Independent gradient model based on Hirshfeld partition: A  
822 new method for visual study of interactions in chemical systems, *Journal of Computa-*  
823 *tional Chemistry*, 43, 539-555, 10.1002/jcc.26812, 2022.
- 824 Lyu, Y., Xu, H., Yuan, H. X., Cui, Y. L., Zhang, C. Z., and Meng, Q. T.: Intermolecular  
825 interaction mechanisms between dinitrophenol and water: a molecular dynamics and  
826 DFT study, *European Physical Journal Plus*, 140, 10.1140/epjp/s13360-025-06478-8,  
827 2025.
- 828 Maeda, S., Harabuchi, Y., Ono, Y., Taketsugu, T., and Morokuma, K.: Intrinsic Reaction  
829 Coordinate: Calculation, Bifurcation, and Automated Search, *International Journal of*  
830 *Quantum Chemistry*, 115, 258-269, 10.1002/qua.24757, 2015.
- 831 Mahilang, M., Deb, M. K., and Pervez, S.: Biogenic secondary organic aerosols: A re-  
832 view on formation mechanism, analytical challenges and environmental impacts,  
833 *Chemosphere*, 262, 10.1016/j.chemosphere.2020.127771, 2021.
- 834 Mangotra, A. and Singh, S. K.: Volatile organic compounds: A threat to the environment  
835 and health hazards to living organisms - A review, *Journal of Biotechnology*, 382, 51-  
836 69, 10.1016/j.jbiotec.2023.12.013, 2024.
- 837 Mao, Y. F., Qin, H., Huang, W. X., Lei, Y. S., Gao, X. J., Zhou, T. H., Wu, D. L., and  
838 Xu, L. Q.: Toward an atomic-scale understanding of competitive adsorption between  
839 ions and molecules near aqueous interfaces, *Chemical Engineering Journal*, 495,  
840 10.1016/j.cej.2024.153699, 2024.
- 841 McNeill, V. F.: Atmospheric Aerosols: Clouds, Chemistry, and Climate, *Annual Review*  
842 *of Chemical and Biomolecular Engineering*, 8, 10.1146/annurev-chembioeng-060816-  
843 101538, 2017.
- 844 Nagy, P. R.: State-of-the-art local correlation methods enable affordable gold standard  
845 quantum chemistry for up to hundreds of atoms, *Chem Sci*, 15, 14556-14584,  
846 10.1039/d4sc04755a, 2024.



- 847 Ohto, T., Dodia, M., Imoto, S., and Nagata, Y.: Structure and Dynamics of Water at the  
848 Water-Air Interface Using First-Principles Molecular Dynamics Simulations within  
849 Generalized Gradient Approximation, *Journal of Chemical Theory and Computation*,  
850 15, 595-602, [10.1021/acs.jctc.8b00567](https://doi.org/10.1021/acs.jctc.8b00567), 2019.
- 851 Perumpully, S. J. and Gautam, S.: Impact of aerosols on atmospheric processes and  
852 climate variability: A synthesis of recent research findings, *Geosystems and Geoenvi-*  
853 *ronment*, 4, 100317, <https://doi.org/10.1016/j.geogeo.2024.100317>, 2025.
- 854 Pillar, E. A., Camm, R. C., and Guzman, M. I.: Catechol Oxidation by Ozone and Hy-  
855 droxyl Radicals at the Air-Water Interface, *Environmental Science & Technology*, 48,  
856 14352-14360, [10.1021/es504094x](https://doi.org/10.1021/es504094x), 2014.
- 857 Pino-Rios, R., Inostroza, D., Cárdenas-Jirón, G., and Tiznado, W.: Orbital-Weighted  
858 Dual Descriptor for the Study of Local Reactivity of Systems with (Quasi-) Degenerate  
859 States, *Journal of Physical Chemistry A*, 123, 10556-10562, [10.1021/acs.jpca.9b07516](https://doi.org/10.1021/acs.jpca.9b07516),  
860 2019.
- 861 Salvador, C. M. G., Tang, R. Z., Priestley, M., Li, L. J., Tsiligiannis, E., Le Breton, M.,  
862 Zhu, W. F., Zeng, L. M., Wang, H., Yu, Y., Hu, M., Guo, S., and Hallquist, M.: Ambient  
863 nitro-aromatic compounds - biomass burning versus secondary formation in rural China,  
864 *Atmospheric Chemistry and Physics*, 21, 1389-1406, [10.5194/acp-21-1389-2021](https://doi.org/10.5194/acp-21-1389-2021), 2021.
- 865 Schaefer, T. and Herrmann, H.: Competition kinetics of OH radical reactions with ox-  
866 ygenated organic compounds in aqueous solution: rate constants and internal optical  
867 absorption effects, *Physical Chemistry Chemical Physics*, 20, 10939-10948,  
868 [10.1039/c7cp08571k](https://doi.org/10.1039/c7cp08571k), 2018.
- 869 Shenghur, A., Weber, K. H., Nguyen, N. D., Sontising, W., and Tao, F. M.: Theoretical  
870 Study of the Hydrogen Abstraction of Substituted Phenols by Nitrogen Dioxide as a  
871 Source of HONO, *Journal of Physical Chemistry A*, 118, 11002-11014,  
872 [10.1021/jp508516c](https://doi.org/10.1021/jp508516c), 2014.
- 873 Shi, K., Mei, X. L., Chen, C. R., and Liu, C. Q.: Impact of atmospheric O<sub>3</sub> and NO<sub>2</sub>  
874 on the secondary sulfates in real atmosphere, *Journal of Environmental Sciences*, 150,  
875 277-287, [10.1016/j.jes.2024.02.019](https://doi.org/10.1016/j.jes.2024.02.019), 2025.
- 876 Shirts, M. R., Pitera, J. W., Swope, W. C., and Pande, V. S.: Extremely precise free



877 energy calculations of amino acid side chain analogs: Comparison of common molec-  
878 ular mechanics force fields for proteins, *Journal of Chemical Physics*, 119, 5740-5761,  
879 10.1063/1.1587119, 2003.

880 Shukla, S. S., Dorris, K. L., and Chikkaveeraiah, B. V.: Photocatalytic degradation of  
881 2,4-dinitrophenol, *Journal of Hazardous Materials*, 164, 310-314, 10.1016/j.jhaz-  
882 mat.2008.08.047, 2009.

883 Spiegel, M., Semidalas, E., Martin, J. M. L., Bentley, M. R., and Stanton, J. F.: Post-  
884 CCSD(T) corrections to bond distances and vibrational frequencies: the power of  $\Lambda$ ,  
885 *Molecular Physics*, 122, 10.1080/00268976.2023.2252114, 2024.

886 Steiner, T.: The Hydrogen Bond in the Solid State, *Angewandte Chemie International*  
887 *Edition*, 41, 48-76, [https://doi.org/10.1002/1521-3773\(20020104\)41:1<48::AID-](https://doi.org/10.1002/1521-3773(20020104)41:1<48::AID-ANIE48>3.0.CO;2-U)  
888 [ANIE48>3.0.CO;2-U](https://doi.org/10.1002/1521-3773(20020104)41:1<48::AID-ANIE48>3.0.CO;2-U), 2002.

889 Sun, J., Mu, Q., Kimura, H., Murugadoss, V., He, M., Du, W., and Hou, C.: Oxidative  
890 degradation of phenols and substituted phenols in the water and atmosphere: a review,  
891 *Advanced Composites and Hybrid Materials*, 5, 627-640, 2022.

892 Sun, Y. N., Yao, J. F., Tang, Y. Z., Zhang, Y. J., Wu, W. Z., and Sun, J. Y.: Theoretical  
893 study on the atmospheric degradation mechanism and subsequent products of E,E-2,4-  
894 hexadienal with hydroxyl radical, *International Journal of Quantum Chemistry*, 121,  
895 10.1002/qua.26563, 2021.

896 Sushko, I., Novotarskyi, S., Körner, R., Pandey, A. K., Cherkasov, A., Li, J., Gramatica,  
897 P., Hansen, K., Schroeter, T., Müller, K. R., Xi, L., Liu, H., Yao, X., Öberg, T., Hor-  
898 mozdiari, F., Dao, P., Sahinalp, C., Todeschini, R., Polishchuk, P., Artemenko, A.,  
899 Kuz'min, V., Martin, T. M., Young, D. M., Fourches, D., Muratov, E., Tropsha, A.,  
900 Baskin, I., Horvath, D., Marcou, G., Muller, C., Varnek, A., Prokopenko, V. V., and  
901 Tetko, I. V.: Applicability domains for classification problems: Benchmarking of dis-  
902 tance to models for Ames mutagenicity set, *J Chem Inf Model*, 50, 2094-2111,  
903 10.1021/ci100253r, 2010.

904 Szatyłowicz, H., Jezuita, A., Ejsmont, K., and Krygowski, T. M.: Substituent Effect on  
905 the  $\sigma$ - and  $\pi$ -Electron Structure of the Nitro Group and the Ring in Meta- and Para-  
906 Substituted Nitrobenzenes, *Journal of Physical Chemistry A*, 121, 5196-5203,



- 907 10.1021/acs.jpca.7b03418, 2017.
- 908 Tam, J. Y. C., Lorschbach, T., Schmidt, S., and Wicker, J. S.: Holistic evaluation of bio-  
909 degradation pathway prediction: assessing multi-step reactions and intermediate prod-  
910 ucts, *Journal of Cheminformatics*, 13, 63, 10.1186/s13321-021-00543-x, 2021.
- 911 Thangamani, D., Shankar, R., Vijayakumar, S., and Kolandaivel, P.: Mechanism and  
912 kinetics of the atmospheric degradation of 2-formylcinnamaldehyde with O<sub>3</sub> and hy-  
913 droxyl OH radicals - a theoretical study, *Molecular Physics*, 114, 3055-3075,  
914 10.1080/00268976.2016.1214293, 2016.
- 915 Tiwari, J., Tarale, P., Sivanesan, S., and Bafana, A.: Environmental persistence, hazard,  
916 and mitigation challenges of nitroaromatic compounds, *Environmental Science and  
917 Pollution Research*, 26, 28650-28667, 10.1007/s11356-019-06043-8, 2019.
- 918 Tomas, A., Olariu, R. I., Barnes, I., and Becker, K. H.: Kinetics of the reaction of O<sub>3</sub>  
919 with selected benzenediols, *International Journal of Chemical Kinetics*, 35, 223-230,  
920 <https://doi.org/10.1002/kin.10121>, 2003.
- 921 Tuñón, I. and Williams, I. H.: Chapter Two - The transition state and cognate concepts,  
922 in: *Advances in Physical Organic Chemistry*, edited by: Williams, I. H., and Williams,  
923 N. H., Academic Press, 29-68, <https://doi.org/10.1016/bs.apoc.2019.09.001>, 2019.
- 924 Tyburski, R., Liu, T. F., Glover, S. D., and Hammarström, L.: Proton-Coupled Electron  
925 Transfer Guidelines, Fair and Square, *Journal of the American Chemical Society*, 143,  
926 560-576, 10.1021/jacs.0c09106, 2021.
- 927 Van Der Spoel, D., Lindahl, E., Hess, B., Groenhof, G., Mark, A. E., and Berendsen, H.  
928 J. C.: GROMACS: Fast, flexible, and free, *Journal of Computational Chemistry*, 26,  
929 1701-1718, <https://doi.org/10.1002/jcc.20291>, 2005.
- 930 vom Eysler, C., Börgers, A., Richard, J., Dopp, E., Janzen, N., Bester, K., and Tuerk, J.:  
931 Chemical and toxicological evaluation of transformation products during advanced ox-  
932 idation processes, *Water Science and Technology*, 68, 1976-1983,  
933 10.2166/wst.2013.452, 2013.
- 934 Wang, C. L., Zhao, N., Ma, Z. J., He, M. X., Hou, C. X., and Sun, J. F.: Unraveling the  
935 heterogeneous reaction of 4-nitrocatechol with ozone in the atmosphere: A combined  
936 DFT, molecular dynamics, and environmental risk assessment, *Atmospheric Research*,



937 331, 10.1016/j.atmosres.2025.108632, 2026.

938 Xing, L., Wu, J., Elser, M., Tong, S., Liu, S., Li, X., Liu, L., Cao, J., Zhou, J., El-Haddad,  
939 I., Huang, R., Ge, M., Tie, X., Prévôt, A. S. H., and Li, G.: Wintertime secondary or-  
940 ganic aerosol formation in Beijing–Tianjin–Hebei (BTH): contributions of HONO  
941 sources and heterogeneous reactions, *Atmos. Chem. Phys.*, 19, 2343-2359,  
942 10.5194/acp-19-2343-2019, 2019.

943 Yan, J. P., Wang, X. P., Gong, P., and Wang, C. F.: Nitrated polycyclic aromatic com-  
944 pounds in the atmospheric environment: A review, *Critical Reviews in Environmental*  
945 *Science and Technology*, 51, 1159-1185, 10.1080/10643389.2020.1748486, 2021.

946 Yang, B., Ren, P. P., Xing, L., Wang, S. H., and Sun, C. L.: Roles of hydrogen bonding  
947 interactions and hydrophobic effects on enhanced water structure in aqueous solutions  
948 of amphiphilic organic molecules, *Spectrochimica Acta Part a-Molecular and Bio-*  
949 *molecular Spectroscopy*, 296, 10.1016/j.saa.2023.122605, 2023a.

950 Yang, B. R., Liang, A. B., and Wang, L. M.: The atmospheric oxidation mechanism of  
951 acetophenone initiated by the hydroxyl radicals, *Atmospheric Environment*, 309,  
952 10.1016/j.atmosenv.2023.119905, 2023b.

953 Young, D., Martin, T., Venkatapathy, R., and Harten, P.: Are the Chemical Structures in  
954 Your QSAR Correct?, *Qsar & Combinatorial Science*, 27, 1337-1345,  
955 10.1002/qsar.200810084, 2008.

956 Zhao, Y. and Truhlar, D. G.: The M06 suite of density functionals for main group ther-  
957 mochemistry, thermochemical kinetics, noncovalent interactions, excited states, and  
958 transition elements: two new functionals and systematic testing of four M06-class func-  
959 tionals and 12 other functionals, *Theoretical Chemistry Accounts*, 120, 215-241,  
960 10.1007/s00214-007-0310-x, 2008.

961